Evidence for Water Ice Near Mercury's North Pole from MESSENGER Neutron Spectrometer Measurements

David J. Lawrence *et al.*

This copy is for your personal, non-commercial use only.

Evidence for Water Ice Near Mercury's North Pole from MESSENGER Neutron Spectrometer Measurements

David J. Lawrence,[1]* William C. Feldman,[2] John O. Goldsten,[1] Sylvestre Maurice,[3] Patrick N. Peplowski,[1] Brian J. Anderson,[1] David Bazell,[1] Ralph L. McNutt Jr.,[1] Larry R. Nittler,[4] Thomas H. Prettyman,[2] Douglas J. Rodgers,[1] Sean C. Solomon,[4,5] Shoshana Z. Weider[4]

Measurements by the Neutron Spectrometer on the MErcury Surface, Space ENvironment, GEochemistry, and Ranging (MESSENGER) spacecraft show decreases in the flux of epithermal and fast neutrons from Mercury's north polar region that are consistent with the presence of water ice in permanently shadowed regions. The neutron data indicate that Mercury's radar-bright polar deposits contain, on average, a hydrogen-rich layer more than tens of centimeters thick beneath a surficial layer 10 to 30 cm thick that is less rich in hydrogen. Combined neutron and radar data are best matched if the buried layer consists of nearly pure water ice. The upper layer contains less than 25 weight % water-equivalent hydrogen. The total mass of water at Mercury's poles is inferred to be 2×10^{16} to 10^{18} grams and is consistent with delivery by comets or volatile-rich asteroids.

E arth-based measurements of radar-bright regions near Mercury's north and south poles were initially reported in 1992 (1), and subsequent measurements showed that these unusual radar characteristics are confined to per-manently shadowed regions within high-latitude impact craters (2). The leading explanation for the high radar reflectance is the presence of large amounts of water ice that can be thermal-ly stable in regions of permanent shadow over geologically long periods of time (2). One of the primary goals of NASA's MErcury Surface, Space ENvironment, GEochemistry, and Rang-ing (MESSENGER) mission is to characterize Mercury's polar regions and thereby identify the principal compositional component of the radar-bright regions. Here we report the results on hy-drogen concentrations near Mercury's north pole from data acquired with MESSENGER's Neutron Spectrometer (NS).

Planetary neutron spectroscopy is a standard technique for remotely measuring planetary hy-drogen concentrations (3). Neutrons are created by nuclear spallation reactions when high-energy cosmic rays strike the surface of an airless or nearly airless planetary body. The energy spectra of the resulting neutrons, which are typically created at energies (E_n) exceeding ~1 to 10 MeV, are typically divided into three energy ranges: fast ($E_n > 0.5$ MeV), epithermal (0.5 eV $< E_n <$ 0.5 MeV), and thermal ($E_n < 0.5$ eV) (Fig. 1A). Hydrogen has a unique ability to moderate neu-trons because hydrogen atoms and neutrons have the same mass, which allows a highly efficient momentum transfer between the two. This effi-cient momentum transfer causes the number of epithermal neutrons to be strongly depressed so that they are highly sensitive to the presence of hydrogen in planetary materials. Fast neutrons are also sensitive to the presence of hydrogen but vary with hydrogen concentration by a factor of 2 less than epithermal neutrons (Fig. 1B). In addi-tion, fast neutrons are sensitive to variations of average atomic mass ($<A>$) in dry planetary ma-terials (4). Finally, fast and epithermal neutrons have different sensitivities to the depth and abun-dance of hydrogen within a hydrogen-rich layer that is covered by tens of centimeters of a hydrogen-poor material. Consequently, combined measure-ments of epithermal and fast neutrons have been used to determine the burial depth of a concen-trated hydrogen layer (5).

The NS is a scintillator-based instrument that separately measures thermal, epithermal, and fast neutrons through a combination of spacecraft Doppler and coincidence pulse processing tech-niques (6). Because of its highly eccentric orbit, the MESSENGER spacecraft is at a moderately high altitude (200 to 600 km) when it passes over or near the radar-bright regions in Mercury's north

[1]The Johns Hopkins University Applied Physics Laboratory, Laurel, MD 20723, USA. [2]Planetary Science Institute, Tucson, AZ 85719, USA. [3]Institut de Recherche en Astrophysique et Planétologie, Université Paul Sabatier–CNRS–Observatoire Midi-Pyrénées, Toulouse, France. [4]Department of Terrestrial Magnetism, Carnegie Institution of Washington, Washington, DC 20015, USA. [5]Lamont-Doherty Earth Observatory, Columbia University, Palisades, NY 10964, USA.

*To whom correspondence should be addressed. E-mail: david.j.lawrence@jhuapl.edu
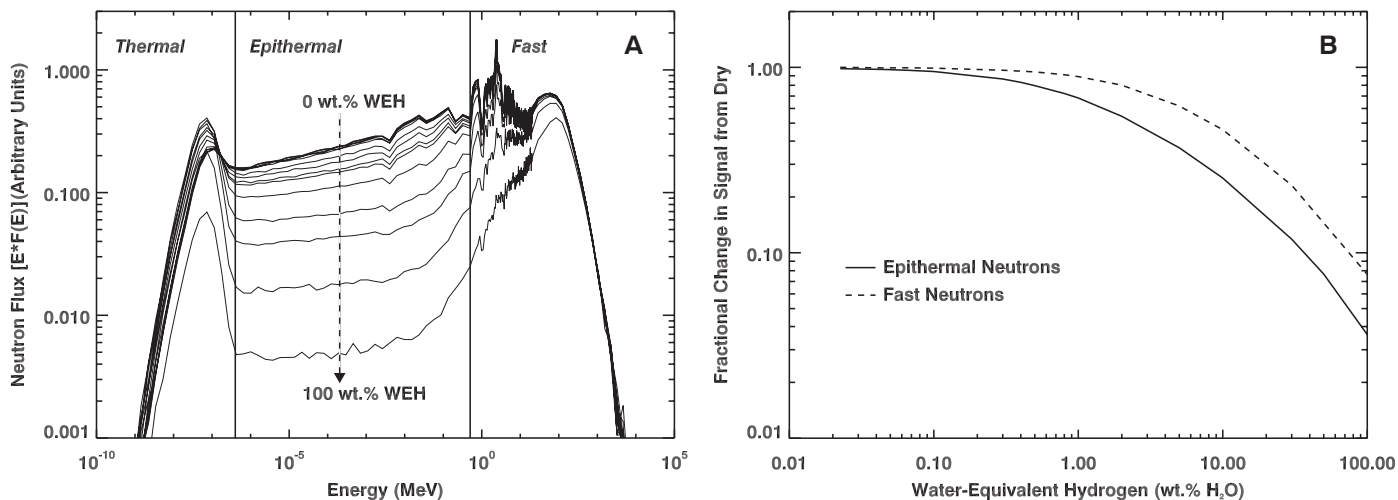
Fig. 1. (A) Simulated neutron flux, plotted as the product of energy and flux versus energy. Simulations were performed with the particle transport code MCNPX for a uniform sphere having Mercury's radius and appropriate soil composition (7, 9) but with a variable concentration of hydrogen from 0 wt % water-equivalent hydrogen (WEH) to 100 wt % WEH. Nominal energy bound-aries for thermal, epithermal, and fast neutrons are shown as vertical lines. **(B)** Simulated relative count rates on the MESSENGER NS for epithermal (solid) and fast (dashed) neutrons as a function of WEH for the same soil composition.

polar region. As a consequence, the omnidirectional neutron measurements have a large spatial footprint (300 to 900 km full-width, half maximum) compared with the size of the radar-bright regions (<40 km), so individual deposits cannot be spatially resolved (7). If extensive water ice is present in the locations of the radar-bright regions, fast and epithermal neutron count rates will show a count rate decrease of 4% or less poleward of latitudes 60° to 70° compared with count rates at lower latitudes (7).

NS data analysis has been carried out with empirically derived corrections applied in parallel with a neutron count rate simulation (8). The count rate simulation, which was validated with flyby data (9), accounts for the near-surface production of neutrons by galactic cosmic rays, their transport to the spacecraft, and their detection by the NS. The simulation was used to guide and constrain the empirical corrections and to provide a capability for bounding the surface hydrogen concentrations. The NS analysis requires corrections to account for nonisotropic solid angle variations, spacecraft obscuration effects, time variations in the incident cosmic ray flux, near-surface temperature variations, and variations from a radial velocity Doppler effect. The radial Doppler effect arises because the speed of the MESSENGER spacecraft in the direction of the spacecraft–planet-center vector has a magnitude (0 to 2 km/s) that is similar to the speed of thermal and low-energy epithermal neutrons (~2 km/s) (10). Doppler-induced effects are negligible for fast neutrons but have a magnitude of a few percent for low-energy epithermal neutrons and therefore need to be considered.

Fully corrected, longitudinally averaged count rates for fast neutrons are shown in Fig. 2 as a function of latitude for data collected from 26 March 2011 to 25 February 2012 (8). Simulated count rates were calculated for the measured count rate collection periods and include all viewing geometry effects. The simulation shows that if the radar-bright regions contain no hydrogen, fast neutrons would display no latitude dependence. In contrast, when a thick surface layer (i.e., having a thickness greater than the depth of sensitivity of the NS) consisting of 100 weight % (wt %) water-equivalent hydrogen (WEH) is included within all mapped radar-bright regions, the simulation shows a poleward decrease of 1.8% in fast neutrons relative to count rates closer to the equator. The NS measurements, in comparison, show a poleward decrease of 1.1% (Fig. 2) (8). When the latitude-dependent signal is averaged over two latitude zones (northward of 75°N and southward of 45°N), the fast neutron count rate at the north pole has a value of 0.9898 ± 0.0020 (two standard deviations, or 2σ) relative to unity at the equator with a statistical significance of 11σ (8). In comparison, simulated count rates with comparable Poisson uncertainties show that if the radar-bright regions were to contain a thick surface layer of 100 wt % water ice, then there would be a 0.978 ± 0.001 (2σ) signal with an 18σ statistical significance (8).

To interpret the fast neutron data, variations in the fast neutron flux unrelated to hydrogen must first be understood. From surface elemental abundances on Mercury (11–15) and assumptions on probable mineralogical assemblages (8), the value of $<A>$ for Mercury's northern volcanic plains (16) may be lower by as much as 0.06 to 0.18 atomic mass unit (amu) than for the surrounding intercrater plains and heavily cratered terrain (8). With the longitudinally averaged data, an $<A>$ decrease in the northern plains is likely to be indistinguishable from a hydrogen signal from radar-bright areas given the broad spatial footprint and limited statistics of the fast neutron data. A 0.06 to 0.18 amu change in $<A>$ corresponds to a 0.6 to 1.8% decrease in relative fast neutron count rate (4). In principle, $<A>$ variations could account for some or all of the fast neutron signal, so that signal is 0.9898 (−0.0020,+0.0102) (8) when all uncertainties are combined.

Two conclusions follow from the polar measurements of fast neutrons. First, the measured polar decrease is a factor of 2 smaller than expected if all radar-bright regions contained pure or nearly pure (80 to 100 wt %) water ice at the surface, so these data do not support the presence of thick surficial deposits of water ice in all radar-bright regions. Second, the regional dynamic range of ~1% for fast neutrons on Mercury is substantially smaller than that measured for Vesta (~10%) (17), the Moon (~38%) (18), or Mars (~300%) (19), where variations in $<A>$ and/or hydrogen dominate. A 1% fast neutron dynamic range therefore places strong constraints on the major-element variability across Mercury's surface on the spatial scale (few hundreds to 1000 km) of the NS footprints.

Fully corrected, longitudinally averaged count rates for epithermal neutrons are shown as a function of latitude in Fig. 3 (8). Data collection times and selections for epithermal neutrons are the same as those for fast neutrons. The monotonic equator-to-pole variation is due mostly to the radial Doppler effect, which is treated in the latitudinally binned count rates by normalizing both the 100 wt % WEH simulation results and the measurements to the no-water simulation rates (Fig. 3B).

The dominant, remaining signal in the measured epithermal neutron data is a decrease at high latitudes, relative to the no-water simulation, that starts near latitude 70°N. The magnitude and latitude profile of this variation closely matches that of the simulated count rate for a thick, surficial layer of 100 wt % water ice at all the radar-bright regions identified from radar observations (2). The good agreement between the data and simulation provides strong evidence that large amounts of hydrogen in the form of water ice are present in Mercury's radar-bright regions. Using the highest-latitude value as the maximum polar signal, the epithermal neutron data show a measured polar signal of 0.976 ± 0.0025 (2σ), relative to an equatorial neutron signal of 1. Despite this strong polar signal, relating the magnitude of the polar decrease of epithermal neutrons to a hydrogen concentration within the radar-bright regions requires careful consideration of other sources of variability within the epithermal neutron data.

Differences between data and simulations that are unrelated to the high-latitude signal have magnitudes of ~0.2 to 0.5% (Fig. 3A), which are at least a factor of 5 smaller than the measured
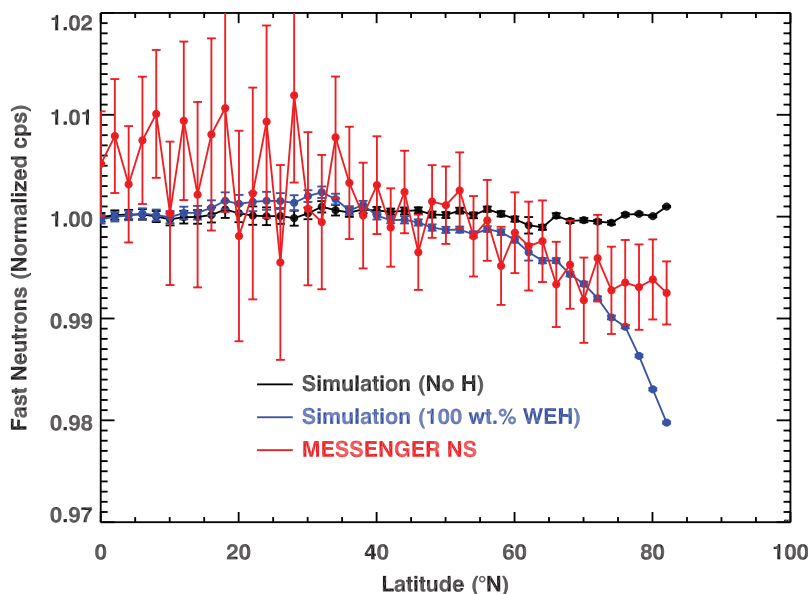
Fig. 2. Measured (red) and simulated (black, blue) fast neutron count rates in units of normalized counts per second (cps) averaged over 2°-wide latitude bins and plotted as a function of latitude. All corrections (8) have been applied. Counts are normalized to the mean count rate (~10 cps) at an altitude of 400 km. Simulated count rates are shown for the cases of no hydrogen (black) and for a thick layer of 100 wt % water ice (blue) located at the surface in all radar-bright regions. The error bars denote twice the measured standard deviation of the mean in each latitude bin.
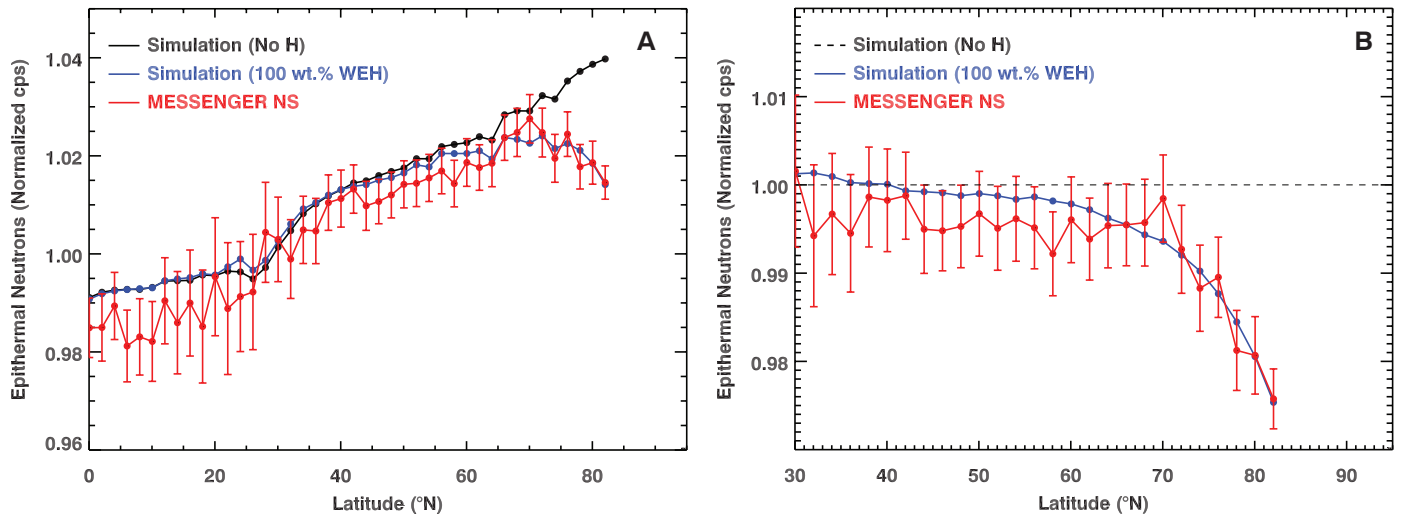
Fig. 3. (**A**) Measured (red) and simulated (black, blue) epithermal neutron count rates averaged over 2°-wide latitude bins and plotted as a function of latitude. All corrections except for a radial Doppler effect have been applied to the data (8). Counts are normalized to the mean count rate (~60 cps) at an altitude of 400 km. Simulated count rates are shown for the cases of no hydrogen (black) and a thick surficial layer of 100% water ice (blue) in all radar-bright regions. The error bars denote twice the measured standard deviation of the mean in each latitude bin. (**B**) Simulated and measured epithermal neutron count rates after correcting for the radial Doppler effect, which is accomplished by normalizing to the simulation with no hydrogen.

latitudinal signal of 2.4%. These differences are most notable at latitudes of 0° to 20°N and 40° to 60°N. These are latitude ranges over which the spacecraft is known to interact with populations of energetic electrons (EEs) on nearly every orbit (20). The presence of small EE events results in a systematic underestimate of the net neutron counts (8). An empirical correction was applied to reduce the magnitude of this effect to give the 0.2 to 0.5% level seen in Fig. 3A. Nonpolar latitude ranges (30° to 40°N and >60°N) over which EE events are largely absent display the best agreement between data and simulations (<0.2%). These combined results provide us with confidence that the simulation accurately represents the data and differences other than the polar effect result from an as yet imperfect correction for EE events that do not strongly affect the polar measurement.

Subsurface temperature variations are a second potential source of variation in the epithermal neutron count rate unrelated to polar hydrogen (21, 22). From subsurface temperature models (23) and the neutron simulations (8), and given that epithermal neutrons are sensitive to temperatures at a product of depth and density equal to ~30 g/cm^2 (21), we estimate that the variations with temperature account for no more than a 0.16% variation between 70°N and 85°N. Thus, although temperature variations might widen the uncertainty limits, the effect is expected to be more than an order of magnitude smaller than the measured polar signal.

The epithermal neutron data alone provide strong evidence that Mercury's north polar radar-bright regions contain high concentrations of hydrogen, consistent with the presence of water ice. If it is assumed that the water ice is located within the radar-bright regions as a single thick layer, then the epithermal neutron data are consistent

with the presence of up to 100 wt % WEH within these regions. That the 2σ uncertainty of the measurements extends to a slightly larger signal than is given for the hydrogen-rich simulation indicates that the epithermal neutron data are consistent with (but do not require) a larger total area than is specified by the known radar-bright regions. In either case, however, the inferred hydrogen concentration with a single-layer assumption is not consistent with the fast neutron data, which exhibit a smaller signal than expected for a single thick layer of water ice. The combined fast and epithermal neutron data indicate that a hydrogen-rich layer is, on average, buried beneath a layer of material noticeably less abundant in hydrogen.

To estimate hydrogen concentrations and burial depth within the radar-bright regions, the neutron signals measured from orbit must be converted to inferred neutron signals at the surface of the radar-bright regions. We used the neutron simulation as a forward model calibration of the measured signals under the assumption that the entire decrease in neutron flux originates from the radar-bright regions. This type of forward modeling technique has been applied and validated with other nuclear spectroscopy measurements involving large spatial footprints (24–26). With the forward model calibration (8), the inferred neutron signals at the surface of the radar-bright regions are 0.39 (−0.13,+0.61) (fast neutrons) and 0.10 ± 0.059 (epithermal neutrons) relative to equatorward values.

The independent fast and epithermal neutron measurements allow us to use a two-layer model with two free parameters constrained by the measurements (average thickness of the upper layer and hydrogen concentration in one of the layers). We considered two end-member models. For model 1, we assumed that the upper layer contains no

hydrogen ($w_{upper} = 0$ wt % WEH), so that the effective thickness (t) of the upper layer, expressed as the product of density and thickness, and the hydrogen content of the lower layer (w_{lower}) are constrained by the data. For model 2, we assumed that the lower layer has $w_{lower} = 100$ wt % WEH, so that the effective thickness and hydrogen concentration of the upper layer are constrained by the data. These layering models represent an average layering structure, and actual layering need not correspond to a uniform two-layer stratigraphy across the NS field of view for all radar-bright regions. A distribution of different layer configurations among or within radar-bright regions can also satisfy the current data.

From modeled neutron fluxes convolved with the respective NS efficiencies, we calculated the relative count rates for fast and epithermal neutrons for a range of hydrogen concentrations and upper-layer thicknesses in the two-layer models. For model 1 (Fig. 4A), $t = 12$ to 47 g/cm^2 and $w_{lower} = 12$ to 100 wt % WEH. For model 2 (Fig. 4B), $t = 12$ to 47 g/cm^2 and $w_{upper} = 0$ to 25 wt % WEH. These results are consistent with an average two-layer stratigraphy in which the hydrogen concentration in the upper layer is 0 to 25 wt % WEH, the hydrogen concentration in the lower layer is 12 to 100 wt % WEH, and the effective thickness of the upper layer is 12 to 47 g/cm^2. If a typical planetary regolith density of 1.5 g/cm^3 is assumed (27), this effective thickness corresponds to a physical thickness of 8 to 31 cm.

Although we have analyzed the NS data in the context of large hydrogen concentrations within Mercury's permanently shadowed regions, other physical distributions of hydrogen can be considered. One possible distribution is a broad area of hydrogen enrichment poleward of ~70°N in which the hydrogen is emplaced in a single
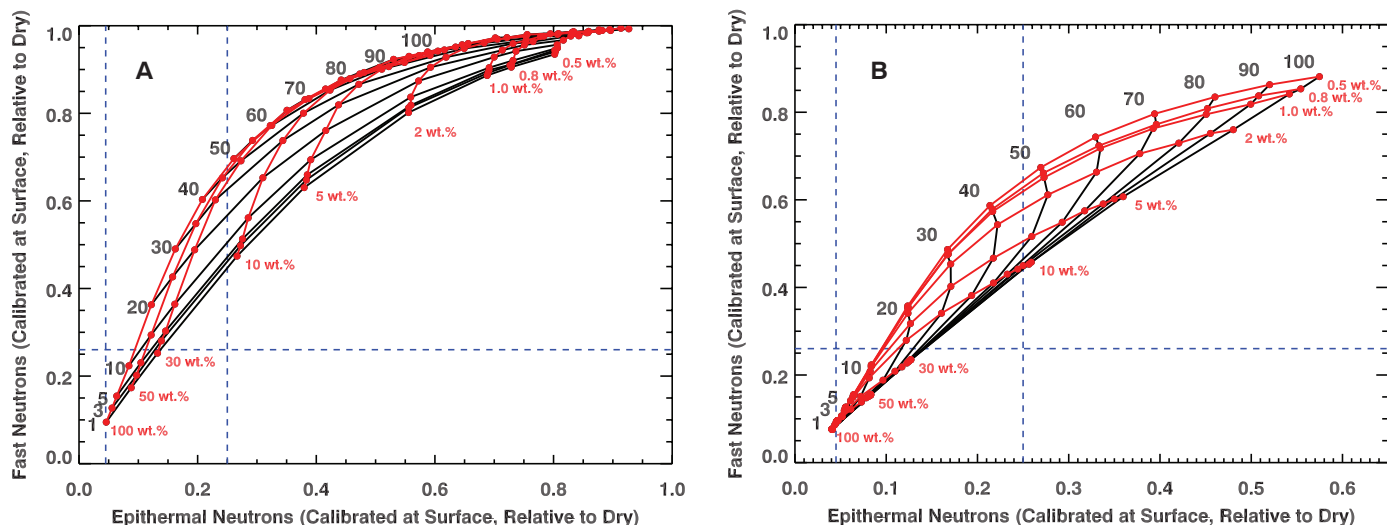
Fig. 4. (A) Simulated epithermal versus fast neutron relative count rates at the surface of the radar-bright regions for a two-layer model stratigraphy (model 1) with a range of values for the thickness of the upper layers and the hydrogen concentration of the lower layer. Black lines and numbers indicate upper-layer thickness contours in units of g/cm². Red lines and numbers indicate contours of lower-layer hydrogen concentrations in units of WEH wt %. Vertical dashed blue lines show the 2σ limits of the calibrated epithermal neutron measurements; the horizontal dashed blue line shows the lower 2σ limit of the fast neutron measurement. The lower and upper thickness values are constrained by the fast and epithermal neutrons, respectively. **(B)** Simulated and measured fast and epithermal neutron count rates for model 2; hydrogen concentration values are shown for an upper layer over a thick layer of 100 wt % water ice.

layer by solar wind. For this scenario, the measured epithermal neutron signal of 2.4% fills the NS field of view, and an average hydrogen concentration can be determined (28) to be 50 parts per million (ppm). The fast neutrons provide few constraints, as the measurement uncertainties allow a hydrogen concentration of 0 to 100 ppm (28). Nevertheless, given the excellent agreement of the epithermal neutron data with the simulation (Fig. 3) along with the strong consistency of the neutron data with other data sets, we consider that the NS observations are better understood as the result of enhanced concentrations of water ice within the radar-bright regions.

The NS results are consistent with observations made by the MESSENGER Mercury Laser Altimeter (MLA) and the Mercury Dual Imaging System (MDIS). Topographic data from MLA, together with thermal models derived from the topography, have shown that for the majority of the north polar radar-bright regions sampled by MLA, water ice is not stable at the surface (23, 29). These studies suggest that any thick water ice layer in these areas is located beneath an insulating layer ~10 cm thick, and MLA reflectance measurements indicate that this surficial layer is darker than surrounding terrain at 1064-nm wavelength and may be enriched in hydrocarbon materials (30). The NS results, which indicate that the upper of the two layers in the north polar deposits has no more than 25 wt % WEH, are consistent with the interpretation that the radar-bright regions contain complex hydrocarbons, possibly mixed with silicate regolith. Images of the north and south polar regions by MDIS (31, 32) have revealed a nearly one-to-one correspondence between radar-bright regions and areas of permanent or at least persistent shadow. Because the

neutron simulations used the same locations of radar-bright features as the illumination studies, the combined results provide a self-consistent basis for interpreting the locations of hydrogen, permanent shade, and radar-bright deposits.

With the identification from neutron spectrometry of large concentrations of hydrogen within the radar-bright regions, it may now be concluded that the high radar backscatter of the polar deposits is the result of nearly pure water ice (2). This consideration favors our model 2, with an assumed hydrogen concentration in the lower layer of $w_{lower} = 100$ wt % WEH. Multiwavelength radar data also support the interpretation that the water-rich layer, on average, is buried beneath an insulating layer of ~10-cm thickness (2). This thickness falls within the range of 8 to 31 cm inferred from the neutron data. The identification of large hydrogen concentrations within the radar-bright regions makes unnecessary such alternative explanations for the high radar backscatter as enhanced concentrations of sulfur (33) or unusual radar properties of silicate materials at low temperatures (34).

Given that the water ice in the polar deposits must be nearly pure, models of surface modification processes (burial and excavation by impacts, loss from ion sputtering and other surface processes, and addition of material from the atmosphere and micrometeoroids) in Mercury's polar region have shown that the bottom layer of deposits must be at least tens of centimeters thick (35). If we use a maximum lower-layer thickness of tens of meters as estimated from models of radar scattering (36) and an estimate of the area of permanent shadow in the north polar region of $(1.25$ to $1.46) \times 10^{14}$ cm² (2), then an estimate of the total mass of water in the north polar region

may be calculated. For a lower-layer thickness in the range 0.5 to 20 m, the total mass of water ranges from 6.2×10^{15} g to 2.9×10^{17} g. If we assume that the radar-reflective regions in the south polar region are also dominantly water ice, then from the area of permanently shadowed regions at high southern latitudes of $(4.3 \pm 1.4) \times 10^{14}$ cm² (32), the total mass of ice in the south polar area ranges from 1.5×10^{16} to 1.1×10^{18} g, and the total mass of ice in both polar regions is 2.1×10^{16} to 1.4×10^{18} g. The total mass could be larger if the lower-layer thickness is greater than 20 m. The mass inferred here is consistent with values estimated earlier (37), and the delivery of this amount of water is possible from the impact of some combination of comets and volatile-rich asteroids onto Mercury (37) followed by migration to the poles with a polar cold-trapping rate of 5 to 15% (38). Models of surface modification that account for vertical and lateral mixing averaged over large areas indicate that a pure water ice deposit will be buried by drier material at a rate of 0.43 cm per million years (My) (35, 39). The average thickness of the upper layer inferred from neutron spectrometry therefore suggests that Mercury's polar water ice was emplaced sometime in the last 18 to 70 My.

Note added in proof: Text has been modified from the version published in *Science* Express (8).

References and Notes

1. M. A. Slade, B. J. Butler, D. O. Muhleman, *Science* **258**, 635 (1992).
2. J. K. Harmon, M. A. Slade, M. S. Rice, *Icarus* **211**, 37 (2011).
3. T. H. Prettyman, Remote chemical sensing using nuclear spectroscopy, in *Encyclopedia of the Solar System*, L. A. McFadden, P. R. Weissman, T. V. Johnson, Eds. (Academic Press, San Diego, CA, ed. 2, 2007), pp. 765–786.

4. O. Gasnault *et al.*, *Geophys. Res. Lett.* **28**, 3797 (2001).
5. W. C. Feldman *et al.*, *Geophys. Res. Lett.* **34**, L05201 (2007).
6. J. O. Goldsten *et al.*, *Space Sci. Rev.* **131**, 339 (2007).
7. D. J. Lawrence *et al.*, *Planet. Space Sci.* **59**, 1665 (2011).
8. Supplementary online material describes the full NS data reduction and analysis.
9. D. J. Lawrence *et al.*, *Icarus* **209**, 195 (2010).
10. W. C. Feldman *et al.*, *Nucl. Instrum. Methods* **A245**, 182 (1986).
11. L. R. Nittler *et al.*, *Science* **333**, 1847 (2011).
12. P. N. Peplowski *et al.*, *Science* **333**, 1850 (2011).
13. S. Z. Weider *et al.*, *J. Geophys. Res.* **117**, E00L05 (2012).
14. P. N. Peplowski *et al.*, *J. Geophys. Res.* **117**, E00L04 (2012).
15. L. G. Evans *et al.*, *J. Geophys. Res.* **117**, E00L07 (2012).
16. J. W. Head *et al.*, *Science* **333**, 1853 (2011).
17. T. H. Prettyman *et al.*, *Science* **338**, 242 (2012).
18. S. Maurice *et al.*, *J. Geophys. Res.* **105**, 20365 (2000).
19. S. Maurice *et al.*, *J. Geophys. Res.* **116**, E11008 (2011).
20. G. C. Ho *et al.*, *Science* **333**, 1865 (2011).
21. R. C. Little *et al.*, *J. Geophys. Res.* **108**, 5046 (2003).
22. D. J. Lawrence *et al.*, *J. Geophys. Res.* **111**, E08001 (2006).
23. D. A. Paige *et al.*, *Science* **339**, 300 (2013); 10.1126/science.1231106.
24. D. J. Lawrence *et al.*, *Geophys. Res. Lett.* **32**, L07201 (2005).
25. J. J. Hagerty *et al.*, *J. Geophys. Res.* **111**, E06002 (2006).
26. T. D. Glotch *et al.*, *Geophys. Res. Lett.* **38**, L21204 (2011).
27. W. D. Carrier III, G. R. Olhoeft, W. Mendell, in *Lunar Sourcebook: A User's Guide to the Moon*, G. Heiken, D. Vaniman, B. M. French, Eds. (Cambridge Univ. Press, 1991), pp. 475–594.
28. W. C. Feldman *et al.*, *Science* **281**, 1496 (1998).
29. There is observational and thermal modeling evidence that a limited fraction of the area of permanent shadow and radar-bright regions contain surficial water ice (*23*, *30*). The neutron data, however, do not have the spatial resolution to distinguish regions of surface ice from the larger areas of shallowly buried ice. Furthermore, multiwavelength radar studies (*2*) suggest that polar deposits in the three largest north polar craters [Chesterton, Tolkien, and Tryggvadóttir (*2*)] that make a large contribution to the overall neutron signal are, on average, buried beneath a thin cover of dry soil or other comparatively ice-poor material.
30. G. A. Neumann *et al.*, *Science* **339**, 296 (2013); 10.1126/science.1229764.
31. N. L. Chabot *et al.*, *J. Geophys. Res.* 10.1029/2012JE004172 (2012).
32. N. L. Chabot *et al.*, *Geophys. Res. Lett.* **39**, L09204 (2012).
33. A. L. Sprague, D. M. Hunten, K. Lodders, *Icarus* **118**, 211 (1995).
34. L. Starukhina, L. V. Starukhina, Y. G. Shkuratov, *Icarus* **147**, 585 (2000).
35. D. Crider, R. M. Killen, *Geophys. Res. Lett.* **32**, L12201 (2005).
36. B. J. Butler, D. O. Muhleman, M. A. Slade, *J. Geophys. Res.* **98**, 15003 (1993).
37. J. I. Moses, K. Rawlins, K. Zahnle, L. Dones, *Icarus* **137**, 197 (1999).
38. B. J. Butler, *J. Geophys. Res.* **102**, 19283 (1997).
39. The surface modification models do not account for thermal effects (*23*) that can operate on time scales much shorter than impact gardening processes (*35*). Thus, the emplacement times implied by the neutron data represent an upper limit.

Bright and Dark Polar Deposits on Mercury: Evidence for Surface Volatiles

Gregory A. Neumann,[1]* John F. Cavanaugh,[1] Xiaoli Sun,[1] Erwan M. Mazarico,[2] David E. Smith,[2] Maria T. Zuber,[2] Dandan Mao,[3] David A. Paige,[4] Sean C. Solomon,[5,6] Carolyn M. Ernst,[7] Olivier S. Barnouin[7]

Measurements of surface reflectance of permanently shadowed areas near Mercury's north pole reveal regions of anomalously dark and bright deposits at 1064-nanometer wavelength. These reflectance anomalies are concentrated on poleward-facing slopes and are spatially collocated with areas of high radar backscatter postulated to be the result of near-surface water ice. Correlation of observed reflectance with modeled temperatures indicates that the optically bright regions are consistent with surface water ice, whereas dark regions are consistent with a surface layer of complex organic material that likely overlies buried ice and provides thermal insulation. Impacts of comets or volatile-rich asteroids could have provided both dark and bright deposits.

Mercury's near-zero obliquity and impact-roughened topography (*1*) prevent direct sunlight from reaching substantial portions of its polar regions. Lacking major convective or conductive sources of heat, the permanently shadowed, near-surface regolith experiences temperatures similar to those of the icy Galilean satellites (*2*). It has long been believed on theoretical grounds that such conditions are favorable to the accumulation of volatiles (*3*, *4*). Even with Mercury's close proximity to the Sun, extremes of daytime temperature are not expected to penetrate regolith to substantial depth, allowing near-surface water ice, if present, to remain stable against sublimation for billions of years (*2*). Such hypotheses were renewed when Earth-based radar observations of Mercury, at wavelengths from 3.6 to 70 cm (*5–9*), revealed regions of high backscatter and depolarization at both poles. Radar observations suggested that depo-

sits of nearly pure water ice up to several meters thick lie at or near the surface. Analysis of altimetry and roughness measurements from the Mercury Laser Altimeter (MLA) (*10*, *11*) on the MErcury Surface, Space ENvironment, GEochemistry, and Ranging (MESSENGER) spacecraft (*12*) indicates that craters hosting radar-bright deposits at high northern latitudes are not anomalously shallow, nor do they display distinctive roughness properties in comparison with craters that lack such deposits (*13*). Consequently, the radar-bright material does not form a thick layer overlying regolith (*13*). A thinner surficial layer containing substantial concentrations of ice would, however, be optically brighter than the surrounding terrain (*14*) and should be detectable by active remote sensing.

We report here measurements with MLA of surface reflectance in permanently shadowed north polar regions of Mercury. The MLA instrument illuminates surface spots 20 to 80 m in diameter at 350- to 450-m intervals (*10*). The receiver system measures threshold-crossing times of the received pulse waveforms at two voltages (*15*). A single low-threshold crossing provides surface elevation, and the timing of the rising and falling signal levels for strong returns at both low and high thresholds enables MLA to estimate the received pulse energy and make active measurements of surface reflectance, r_s, via the lidar link equation (*16*, *17*) and preflight sensor calibrations (*10*).

During its primary mapping mission, MESSENGER orbited Mercury in an eccentric orbit with a 12-hour period and a ~200- to 400-km periapsis altitude at 60° to 70°N. In this orbit, the MLA ranged to Mercury from 29 March 2011

[1]NASA Goddard Space Flight Center, Code 698, Greenbelt, MD 20771, USA. [2]Department of Earth, Atmospheric, and Planetary Sciences, Massachusetts Institute of Technology, Cambridge, MA 02139, USA. [3]Sigma Space Corporation, Lanham, MD 20706, USA. [4]Department of Earth and Space Sciences, University of California, Los Angeles, CA 90095, USA. [5]Department of Terrestrial Magnetism, Carnegie Institution of Washington, Washington, DC 20015, USA. [6]Lamont-Doherty Earth Observatory, Columbia University, Palisades, NY 10964, USA. [7]The Johns Hopkins Applied Physics Laboratory, Laurel, MD 20723, USA.

*To whom correspondence should be addressed. E-mail: gregory.a.neumann@nasa.gov